arXiv:1408.0236v1 [astro-ph.SR] 1 Aug 2014

A FLARE OBSERVED IN CORONAL, TRANSITION REGION AND HELIUM I 10830 Å EMISSIONS

Zhicheng Zeng[1,2], Jiong Qiu[3], Wenda Cao[1,2], and Philip G. Judge[4]

1.Center for Solar-Terrestrial Research, New Jersey Institute of Technology, 323 Martin Luther King Blvd., Newark, NJ 07102, USA

2. Big Bear Solar Observatory, 40386 North Shore Lane, Big Bear City, CA 92314, USA

3. Department of Physics, Montana State University, Bozeman, MT 59717-3840, USA

4. High Altitude Observatory, National Center for Atmospheric Research, Boulder CO 80307-3000, USA

ABSTRACT

On June 17, 2012, we observed the evolution of a C-class flare associated with the eruption of a filament near a large sunspot in the active region NOAA 11504. We obtained high spatial resolution filtergrams using the 1.6 m New Solar Telescope at the Big Bear Solar Observatory in broad-band TiO at 706 nm (bandpass: 10 Å) and He I 10830 Å narrow-band (bandpass: 0.5 Å, centered 0.25 Å to the blue). We analyze the spatio-temporal behavior of the He I 10830 Å data, which were obtained over a $90''\times90''$ field of view with a cadence of 10 sec. We also analyze simultaneous data from the Atmospheric Imaging Assembly and Extreme Ultraviolet Variability Experiment instruments on board the Solar Dynamics Observatory spacecraft, and data from Reuven Ramaty High Energy Solar Spectroscopic Imager and GOES spacecrafts. Non-thermal effects are ignored in this analysis. Several quantitative aspects of the data, as well as models derived using the "0D" Enthalpy-Based Thermal Evolution of Loops model (EBTEL: Klimchuk et al. 2008) code, indicate that the triplet states of the 10830 Å multiplet are populated by photoionization of chromospheric plasma followed by radiative recombination. Surprisingly, the He II 304 Å line is reasonably well matched by standard emission measure calculations, along with the C IV emission which dominates the AIA 1600 Å channel during flares. This work lends support to some of our previous work combining X-ray, EUV and UV data of flares to build models of energy transport from corona to chromosphere.

Subject headings: Sun: chromosphere — Sun: transition region — Sun: corona — Sun: flares — Sun: infrared

1. INTRODUCTION

The spectra of helium atoms and ions in the Sun are not yet understood. The EUV resonance lines at He I 584 Å and He II 304 Å respectively are anomalously bright, under

quiescent conditions, by factors of several when compared with many other lines (Jordan 1975, 1980; Zirin 1975; Pietarila & Judge 2004; Judge & Pietarila 2004). Yet, these lines are some of the strongest EUV features in the solar spectrum, and as such they control to a significant degree the state of the earth's thermosphere and ionosphere. Until a clear understanding of the formation of these lines is available, attempts to model the EUV irradiance using models based upon the standard assumption of ionization equilibrium are doomed to fail. In the present study we analyze the evolution of flare emissions in EUV and UV radiation and emission from neutral and ionized helium, to probe the mechanisms leading to the strong helium emission. A broader goal of the present paper is to understand the evolution of the emitting plasmas during flares. We use the narrow-band tunable filtergraph for the New Solar Telescope at the Big Bear Solar Observatory (NST/BBSO; Goode & Cao 2012; Cao et al. 2010b) to capture flare emission in the 10830 Å line. By combining these data with those of the adjacent chromosphere and corona seen at UV and EUV wavelengths with the Atmosphere Imaging Assembly (AIA; Lemen et al. 2012) and Extreme Ultraviolet Variability Experiment (EVE; Woods et al. 2012) instruments on the *Solar Dynamic Observatory* (*SDO*; Pesnell et al. 2012), we use the observed behavior to constrain the mechanisms by which helium emission can occur during flares.

Ground-based observations of helium lines that follow the evolution of flares are not common, the emission being confined to narrow kernels that are ill-suited to observation using slit spectrographs. Some important work by Tandberg-Hanssen (1967) found that in the weaker flares He I 10830 Å shows absorption and only class 2B and larger flares show He I 10830 Å emission. Later, He I 10830 Å emissions were observed in a C9.7 flare with spectro-polarimetry (Penn & Kuhn 1995). Using an infrared (IR) spectrograph with a spatial resolution of 1.″34 and a temporal cadence of 2.8 s, Li et al. (2007) found that only when the GOES X-ray flux (which is integrated over the solar disk) reaches a threshold (about C6 class in their study) could they detect emission exceeding the continuum, which spatially corresponded to a bright Hα kernel.

Kleint (2012) has analyzed data of photospheric Fe I 6302 Å and chromospheric Ca II 8542 Å lines in a C3 class flare. She finds that emission occurs only above the photosphere, within chromospheric plasma. It should be remembered that the chromosphere spans some 9 pressure scale heights between the quiescent (pre-flare) photosphere and overlying corona. These facts are suggestive that the He I 10830 Å emission should also arise from the chromospheric layers inside the flare footpoints.

Any process that can excite helium leading to line radiation requires a change in principle quantum number n from the $n = 1$ ground levels. Thus helium excitation is unusually sensitive to *high energy tails in distribution functions of the radiation field and/or plasma electrons and ions*. For example, the resonance lines ($2s - 2p$) of C IV have a 5x lower threshold than the resonance line of He II ($1s-2p$) which form at similar temperatures, under ionization equilibrium conditions. One proposal uses "high energy photons" (shortward of 228

and 504 Å) to ionize ionized/neutral helium from which recombination populates the $n = 2, 3$ levels of helium (Zirin 1975). By solving the standard non-LTE radiation transfer problem in 1D semi-empirical models of the solar atmosphere, it is found that the properties of the He I 10830 Å multiplet depend mainly on the density and the thickness of the chromosphere, as well as on the incoming EUV coronal back-radiation. (Pozhalova 1988; Avrett et al. 1994; Centeno et al. 2008).

Another appeals to the diffusion of helium atoms and ions up steep temperature gradients where the locally higher temperature can excite the $n = 2$ levels faster than occurs for transitions such as the C IV resonance lines (Jordan 1975). Yet another uses unresolved plasma motion to achieve the same result (Andretta et al. 2000). Flare spectra of EUV helium emission lines, observed with the SO82A (spectroheliograph, or "overlap-ogram") instrument, were analyzed in terms of a "burst" model by Laming & Feldman (1992). Laming & Feldman (1992) assumed that, during flares, "ionizing plasma" conditions exist in the Sun's transition region, permitting the excitation of $n = 2, 3$ levels before ionization occurs. Pietarila & Judge (2004) showed that all of these mechanisms can be unified into a common picture of excitation, by considering the conditions experienced by the motions of individual atoms and ions of helium (Lagrangian picture).

No matter the precise mechanism at play, helium may be expected to shed light on processes requiring much higher energies (> 10 eV) than are present throughout the bulk of the chromosphere (~ 0.6 eV). Near simultaneous observations of various photospheric and chromospheric lines show that the chromosphere is the location of the footpoint emission from at least moderate (C-class) flares (Kleint 2012).

Furthermore, the importance of He I 10830 triplet is being realized from monitoring dynamical activity in the chromosphere and measuring the chromospheric magnetic fields. Trujillo Bueno & Asensio Ramos (2007) have modelled the scattering polarization by interpreting the observed polarization in terms of the Zeeman and Hanle effects.

We proceed by combining high angular resolution observations of the He I 10830 Å multiplet with lower resolution measurements of He II 304 Å obtained with SDO. Other observables from SDO, as well as X-ray emissions from the *Reuven Ramaty High Energy Solar Spectroscopic Imager* (*RHESSI*; Lin et al. 2002) and GOES will be used to understand the changing conditions in the emitting chromospheric and coronal plasma.

2. OBSERVATIONS

With the advent of the 1.6 meter NST at the BBSO, ground based IR observations with high resolution ($\frac{\lambda}{D} \sim 0\farcs14$ in 10830 Å are now regularly acquired. The off-axis design of NST reduces stray light since there is no central obscuration, and the site's good seeing conditions

combined with the high order adaptive optics (AO) have enabled us to obtain observations with a spatial resolution close to the diffraction limit of the telescope. On June 17, 2012, we observed a small filament eruption and the associated flaring activity. One footpoint of the filament was embedded in a small pore near a large sunspot in the active region NOAA 11504. High spatial resolution filtergrams were obtained in a broad band (bandpass: 10 Å) containing well-known TiO lines, and in a narrow band (bandpass: 0.5 Å) in the blue wing of the He I 10830 Å multiplet. The latter images enabled us to establish the photospheric underpinning of the filament in the chromosphere and corona.

2.1. Infrared Data

Our TiO images have a cadence of 30 seconds, with a field-of-view (FOV) of 70″ × 70″. The image scale is 0.″0375/pixel. TiO molecular bands are unusually sensitive to the photospheric temperature, they exhibit enhanced intensity contrast in the photosphere due to the stronger absorption of these bands in cool intergranular lanes. The 10830 Å Lyot filter was made by the Nanjing Institute for Astronomical and Optical Technology. This narrow-band filter was tuned to -0.25 Å relative to the two blended strongest components of the multiplet (at 10830.3 Å), making the filtergram more sensitive to upward moving features. A high sensitivity HgCdTe CMOS IR focal plane array camera (Cao et al. 2010a) was employed to acquire the 10830 Å data with a cadence of 10 seconds. The pixel size of the filtergrams is 0.″0875, and the FOV is 90″ by 90″. With the aid of high order AO (Cao et al. 2010b) and speckle reconstruction post-processing (KISIP speckle reconstruction code, Wöger & von der Lühe 2007), images with diffraction limited resolution at different bands were achieved. All NST data used in this paper are speckle reconstructed. More technical detail in data acquisition and reduction can be found in Cao et al. (2010c).

With the NST we observed the active region continuously for a few hours in good seeing conditions, providing a unique opportunity to follow the entire evolution of the flare with high spatial and temporal resolutions. A movie (NST_flare_20120617.mpg) is available in on-line journal. Observations started before 17:00 UT, well before the flaring activity. Figure 1 is a snapshot of the 10830 Å filtergram during the maximum of the flare, with the bandpass shown in the lower right panel. Since the bandpass is tuned to the blue wing of 10830 Å, the filtergram captures some underlying continuum radiation, with photospheric features including sunspots, pores, and granules clearly visible in the image. The filament appears as a dark feature lying between two large sunspots. During the flare, impulsive brightenings in this bandpass are observed at a few locations, marked as patches 0 to 8 in the figure; these patches will be described as P0 - P8 in the following analysis.

2.2. Supporting Data from SDO and RHESSI

We also take advantage of the SDO's unique continuous coverage of the Sun. We analyze UV and EUV images observed by AIA, and full disk continuum images and line-of-sight (LOS) magnetograms from the Helioseismic and Magnetic Imager (HMI; Schou et al. 2012). AIA takes full-disk images in 7 EUV bands with a cadence of 12 s and spatial scale of 0.″6. These EUV telescopes observe emission from coronal plasmas at temperatures from 1 to 10 MK. Apart from these EUV channels, AIA also takes full-disk images at the UV 1600 Å broadband at 24 s cadence. During flares, the C IV doublet is significantly enhanced to dominate emission in this band (Qiu et al. 2012), also confirmed in the present analysis. The C IV line emission is produced by plasmas near 100,000 K, typical of the mid transition region.

Spatial co-alignment among these data is done by first co-aligning the HMI continuum images with the NST TiO data. Using the granular patterns and sunspots, it is straightforward to precisely align the HMI/SDO continuum images with the NST TiO images. Then we co-align the TiO data with the 10830 Å filtergrams using the sunspots and bright granules. AIA and HMI observations are co-aligned with each other using satellite pointing information, and the HMI continuum images serve as the intermediary for co-alignment between the AIA images and the NST images. The accuracy of the co-alignment is better than 0.″5.

Finally, X-ray emission of the flare are also observed by GOES and RHESSI. Using the standard RHESSI software package, we obtain RHESSI X-ray light curves and images with pixel size of 2.26″ by 2.26″ (subcollimators 1, 3, 4, 5, 6, 8 are used). The RHESSI data are co-aligned with the SDO data according to the coordinates provided in the FITS header. Light curves and images of the flare in the X-ray, EUV, UV, and IR wavelengths are illustrated in Figure 2 and Figure 3 respectively, derived as discussed below.

2.3. Overview of the Flare

In the top panel of Figure 2, X-ray light curves in several RHESSI channels and in GOES 1-8 Å channel are plotted[1]. Colored curves in panel (b) of Figure 2 show normalized light curves in several wavelengths: the IR 10830 Å from NST, EUV bands at 94 Å and 171 Å from AIA/SDO, and UV band at 1600 Å also from AIA/SDO. In panel (b), the 1600 Å light curve (green) is created from total counts of selected footpoint pixels that exhibit strong emission, or more specifically those pixels with a count rate greater than five times the median count rate ($I_q = 71\ DNs^{-1}$) of the quiescent region. Since the AIA data and NST data have been well co-aligned, the light curve of He I 10830 Å (black) is made from the counterpart of the footpoint pixels in 1600 Å. The light curves in EUV 94 Å (blue) and 171 Å (red) are made

[1]Note that 10 keV corresponds to a photon wavelength of 1 Å.

from pixels of the entire FOV shown in Figure 3. Each curve is subtracted by its minimum values and then divided by the residual maximum. As seen in Figure 2, flaring occurs in two phases, with the SXR emission in GOES 1-8 Å peaking at 17:28 UT and 17:39 UT, respectively. Each phase is usually characterized by a rapid rise of the emission, followed by a more gradual decay. Remarkably, we find that emission in the IR and UV bands peaks first, along with a peak in the 171 Å channel, immediately followed by SXR emissions by relatively high temperature plasmas, and then by lower temperature EUV emissions in 94 Å (6 MK) and 171 Å (1 MK). For the EUV 171 Å light curve, the first two peaks coincide with the UV and IR peaks while the following ones correspond to the cooling of the post-flare coronal loops.

Figure 3 shows the evolving morphology of flaring plasma observed in several wavelengths. Before the flare onset, twisting of the dark filament can be seen in the 10830 Å filtergrams (see panel a1 of Figure 3 and the on-line movie (NST_flare_20120617.mpg)). Before the flare is seen in X-ray, the filament is dark in 10830 Å filtergram as shown in panel a1 and there are no obvious signals in EUV images. However, in UV 1600 Å images (b1), there are brightenings right in the middle of the filament, indicating the ongoing activity at upper chromosphere prior to the filament eruption and flare. These small events account for a minor emission peak at 17:22 UT before the flare as shown in Figure 2. Next, the filament brightening and eruption (second column in Figure 3) are coincident in time with the first major abrupt rise in the light curves. Ten minutes later, a second abrupt brightening phase (third column in Figure 3) was observed as the emission of the footpoint dramatically increases. The intensity of 10830 Å is significantly enhanced by more than 50% of pre-flare state.

In the top panels of Figure 3, contours of the X-ray images by RHESSI are overlaid on the 10830 Å images. Strong soft X-ray (SXR) emission at photon energies from 6-15 keV (green contours) is observed during both phases of the flare, from an extended coronal emission source lying above the foot-point patches significantly larger than the SXR RHESSI angular resolution ($\sim 2-3''$), also shown in Figure 3(a2-a3). There is also a small amount of X-ray emission above 25 keV, most likely the hard X-ray (HXR) emission (red contours), which is present for only a short time. So these weak signals above 25 keV suggest that the non-thermal effects are not significant in this event (Fletcher et al. 2011, section 2.4). The SXR emissions below 25 keV and in GOES 1-8 Å channel are usually produced by flare plasmas heated to over 10 MK (Hannah et al. 2008).

During these two major phases of the flare, emissions in IR, UV, and EUV bands occur in the localized patches, P0-P8, which are connected by coronal loops brightened later on in 131 Å (e4) and 171 Å (d4). Therefore, these IR and UV bright kernels most likely correspond to footpoints of flare loops. The counterpart in the corona is shown in both 171 Å and 131 Å images (d1-e4), reflecting the loop structures with million degree plasma. EUV flux observed by AIA are saturated in 171 Å and 131 Å, especially during the first impulsive phase. In

the first impulsive phase, the saturations are in the middle of the filament which is shown in the column a2-e2 of Figure 3, and they coincide with both the RHESSI SXR contour and chromospheric brightenings in 1600 Å and 10830 Å. Then during the second peak, the footpoints become bright. These observations strongly suggest that the filament eruption starts from chromosphere (early activity in AIA 1600 Å inside filament) and when magnetic reconnection happens, the released energy heats the plasma to the coronal temperature (SXR and EUV brightening in the first impulsive phase). Later, magnetic reconnection takes place in the disturbed corona, giving rise to more energy release and formation of new coronal loops as well as brightened foot-points; this generates the second phase of the flare. (The whole process is also seen in the on-line movie.).

Figure 4 shows the TiO images during the flare as well as one HMI photospheric magnetogram, showing only LOS components of the magnetic field. Blue contours superimposed in these images are IR foot-point patches brightened during the flare. The TiO images exhibit lots of small-scale bright points, but barely any enhanced flare emission at the locations of the bright IR patches. Therefore, we can assert that *the foot-point brightening observed in the He 10830 Å band is not produced in the photosphere*. The panel (c) in Figure 4 shows one (typical) HMI LOS magnetogram. The blue and red contours are footpoint patches of the 10830 Å filtergram and coronal loop of the AIA 131 Å image, respectively. Further, the IR footpoint patches are located in penumbral magnetic fields with different polarity and most of them are seen to be connected by coronal loops. Patches P0, P1, P2, and P5 are located in magnetic fields of negative polarity, while P3, P4, P6, P7, and P8 are located in positive polarities. The loops in the AIA 131 Å seem to connect P0-P2 to P3-P4, and P5 appears to be connected with P6. These loops are significantly inclined relative to the magnetic polarity inversion line.

2.4. Light Curves of Flare Foot-point Emission

In Figure 5, we plot light curves of P0, P4, and P6 in 10830 Å, AIA 1600 Å and 304 Å, these being typical examples. The GOES 1-8 Å light curve is not plotted since it is not spatially resolved. The patches are rectangular areas containing a combined 906 AIA pixels (each with scale of $0\farcs6$) that are centered over the enhanced 10830 Å regions brightened during the flare (see Fig. 1). In Figure 5 we have subtracted minimum values for each curve and then divided the curves by their residual maximum.

In this paper, the IR filtergram contains both line wing and part of the line center of the He I 10830 Å and the line profile before the flare is in absorption. Approximations at the footpoint are made as follows:

1. Before the flare, the clear view of the penumbra indicates the absorption is optically thin and only a small fraction of continuum flux is absorbed. Hence the observed flux

before flare may be approximated as continuum.

2. The flare in this paper is not a white-light flare so the quiescent (pre-flare) continuum is the same as continuum during flare, which means that the emission enhancement is due to He I 10830 Å;

3. Therefore we assume that the flare enhancement with respect to pre-flare flux is approximately the same as enhancement over the quiescent continuum.

Figure 6 shows the histogram of the peak intensity, normalized to the pre-flare emission, of these 906 pixels in different wavelengths. The UV 1600 Å and EUV 304 Å flare emissions have increased by up to two orders of magnitude, and the IR intensity has grown by a factor of 1.2 to 2.5 over the pre-flare emission. It is noteworthy that, previous flare observations in the He I 10830 Å bandpass have shown IR darkening (Harvey & Recely 1984) and only when the GOES X-ray flux reaches a threshold could they detect emission (Tandberg-Hanssen 1967; Li et al. 2007). However, in this flare, almost all flaring pixels exhibit IR emission even during the first phase when GOES 1-8 Å emission is only at C1 level.

As shown in Figure 5, the emissions from P0, P4, P6 in 10830 Å, 1600 Å and 304 Å all rise rapidly on the same timescale, and peak at the same time; they then decay more gradually but with quite different timescales: the 304 Å emission decays slightly slower than the 1600 Å emission, and the 10830 Å IR intensity decays most slowly. Similar behavior is seen in individual pixels but with lower signal to noise ratios. The statistics of rise and decay timescales of all pixels are plotted in Figure 7. For each pixel, the maximum of light curve is recorded. Then the light curve from the onset of the flare to the time of maximum is fitted using a half Gaussian function. The rising timescale is calculated as half of the full width at half maximum of the fitted Gaussian function. Then the curve from maximum is fitted to an e-slope. The decay timescale is calculated from the time of its maximum to the time when it decays to $\frac{1}{e}$ of its maximum.

The flux of most pixels rise impulsively within one minute. The UV 1600 Å flux typically decays within a few minutes while the decay timescale of the 304 Å flux is around 10 minutes. The flux in 10830 Å decays on longer timescales of a few tens of minutes.

3. ANALYSIS

3.1. Summary of Critical Observations

There are several critical aspects to IR 10830 Å narrow-band and other data (refer to Figures 1-7) which we highlight and will draw upon below:

1. The 10830 Å emission is confined to patches that are mophologically a mixture of bright

fibril-like structures (P1, P5, P7), and bright amorphous patches (P0, P2, P3, P6, P8) (Figure 1).

2. These patches lie mostly over penumbral regions, on large scales they are associated with bright UV/EUV emission (Figure 4).

3. The 10830 Å emission often has sharp edges (e.g. P0), close to the resolution limit of the observations (0.″14) (Figure 1).

4. The SXR emission observed below 15 keV by RHESSI is from a much extended source: in contrast to the sharp edges in 10830 Å (Figure 3).

5. The simultaneous steep rise at 304, 1600 and 10830 Å footpoint emissions suggests that the IR and UV/EUV emissions are related during this phase (Figure 5).

6. The 10830 Å emission decays an order of magnitude more slowly than other UV/EUV emission, but has some similarity to the RHESSI and GOES decay curves (Figure 2).

3.2. Physical picture

In previous work Qiu et al. (2012) have found a simple physical picture which can account for the UV and EUV data of flares that are qualitatively similar to the new observations presented here. Some process to be identified transfers energy rapidly out of the corona. When this energy is directed towards the lower solar atmosphere then this atmosphere responds by trying to deal with the excess energy through ionization, radiation losses, fluid motions and perhaps other modes (MHD waves, particle acceleration).

Evolution of plasma at the feet of flare loops begins with a highly dynamic response to impulsive heating. In work by Qiu et al. (2012), the "impulsive rise"[2] of the UV 1600 Å light curves at the flare foot-points is used to estimate empirical heating rates through a "0D" model. The method, using only two free parameters, has been applied to analyze and model heating of thousands of flare loops in a few flares with agreeable comparison between synthetic and observed X-ray and EUV spectra and light curves (Qiu et al. 2012; Liu et al. 2013; Li et al. 2014). Using UV signatures to build heating rates, these studies not only resolve heating in individual loops but are not confined to flares that have significant thick-target HXR emissions. In the present paper, we make two further simplified assumptions based upon previous work (Qiu et al. 2012) and upon the weakness of HXR emissions: (1) the 1600 Å emission during the flare is dominated by C IV emission and not the underlying continuum; (2) there are no significant non-thermal particles impacting the solar chromosphere from above.

[2]Not to be confused with the "impulsive" phase of many flares seen at radio and gamma ray wavelengths.

The thermal conduction from the site of energy deposition will generate a downward propagating shock front, which most likely produces the impulsive spike in the UV and EUV light curves (Fisher 1989). On the other hand, the cooling of the overlying corona governs the gradual decay. Such two phase evolution in the UV emissions has been reported by Hawley et al. (2003) in stellar flare observations, and they found that during the cooling phase, a few lines including C IV can be used as a transition region pressure gauge monitoring the coronal plasma evolution in overlying flare loops. The differential emission measure (DEM) throughout the transition region is proportional to the equilibrium coronal pressure since the entire loop is in approximate hydrostatic balance in the cooling phase (Fisher 1987; Griffiths et al. 1998; Hawley & Fisher 1992). In this "pressure-gauge" approximation, the decay phase of UV/EUV emission in solar flares (Liu et al. 2013; Qiu et al. 2013) also compares favorably with the observations. Here, we adopt this model to compute decay-phase flare foot-point emission in EUV He II 304 Å, and UV C IV bands. The IR He I 10830 Å emission is then studied in the context of this model. Below, we model plasma evolution in hundreds of flare loops observed in this flare to find the coronal/transition region structure overlying the IR patches. We then estimate He I 10830 Å enhancement due to different physical processes in these patches to compare with observations.

3.3. Calculations with EBTEL

For loops during the decay phase in approximate hydrostatic balance, the DEM throughout the transition region is proportional to the equilibrium coronal pressure and the optically thin radiative losses are balanced by the downward conductive heat from the cooling coronal loops. With the plasma flow neglected, the DEM along the leg of the flux tube is computed analytically (Fisher 1987; Griffiths et al. 1998; Hawley & Fisher 1992) as

$$\xi_{se}(T) = \overline{P}\sqrt{\frac{\kappa_0}{8k_B^2}}T^{\frac{1}{2}}Q^{-\frac{1}{2}}(T)$$

where

$$Q(T) = \int_{T_0}^{T} T'^{\frac{1}{2}}\Lambda(T')dT'$$

and $\Lambda(T)$ is the optically thin radiative loss function. κ_0 is the thermal conductivity coefficient and k_B is Boltzmann constant. Expressing the temperature-dependent scaling constant as $g_{se}(T)$, the transition region DEM can be computed as $\xi_{se}(T) = g_{se}(T)\overline{P}$, which is directly proportional to the mean pressure $\overline{P}$ calculated using the zero-dimensional loop heating model, the enthalpy-based thermal evolution of loops model (EBTEL; Klimchuk et al. 2008;

Cargill et al. 2012a,b). Qiu et al. (2013) and Liu et al. (2013) have already confirmed that this pressure-gauge approximation can re-produce observed gradual decay reasonably well.

We have used the spatially resolved AIA 1600 Å light curves to determine the empirical heating rates of the observed flare loops. With these heating rates, a zero-dimensional EBTEL model is used to compute mean temperature and density of plasmas in these flare loops. EBTEL solves an energy equation and a mass equation, taking into account an ad-hoc heating term which we infer from foot-point UV light curve, coronal radiative loss, the loss through the transition region which in this study is scaled to the pressure of the coronal plasma, and thermal conduction and enthalpy flow between the corona and transition region. The synthetic coronal radiation in SXR and EUV bands are then computed and compared with observations by GOES and AIA to verify the very few parameters in the method.

Results of EBTEL calculations for the present datasets are shown in Figure 8. Using the 906 UV brightened pixels seen with SDO we have modeled 906 half loops anchored to these pixels. The lengths of these half loops are estimated from the EUV images, which range from 16 to 41 Mm. The heating rates of these loops are assumed to be proportional to the rise of the UV light curve at the foot-point pixel with a constant scaling factor which can be adjusted by best matching synthetic and observed EUV light curves. For this flare, the inferred heating rate in the 906 half loops ranges from 1×10^{8} to 7.5×10^{11} ergs s^{-1} cm^{-2}, and the total heating rate is plotted as dashed line in the top left panel of Figure 8 together with the UV total counts light curve. By assumption we ignore beam heating scenarios and assume that (non-radiative) magnetic heating primarily occurs in the corona. The other panels in the figure show synthetic SXR and EUV light curves in comparison with those observed by GOES 1-8 Å and 6 EUV bandpasses of AIA. Light curves in these passbands reflect evolution of coronal plasmas that are heated to over 10 MK and then gradually cool down to 1-2 MK. As shown in Figure 8, the synthetic light curves reflect the cooling of the flare, with high temperature emissions (131 and 94 bands) peaking earlier than low-temperature emissions (211, 193, and 171 bands). The synthetic and observed light curves coincide with each other quite well: they exhibit very similar time profiles and the magnitude of the total counts are comparable by within a factor of 2. The good comparison indicates that the method is able to reproduce mean properties of the corona during the flare.

In these models, the plasma pressure at the coronal base increases from a pre-flare state between 0.1 and 1 dyne cm^{-2} up to pressures of several times 10^{1-2} dyne cm^{-2} during the flare. Accordingly, the emission from lines such as C IV increases by similar factors. The underlying UV continuum near 1600 Å, however, forms near pressures closer to $1-2\times10^{3}$ dyne cm^{-2} under quiescent conditions (Vernazza et al. 1981), over an order of magnitude higher. Thus, we would expect downward propagating flare energy to be attenuated before it can reach such high pressures, associated with the much deeper "temperature minimum" region below the chromosphere.

Our observations show that the brightest IR 10830, UV 1600, and EUV 304 emission are generated in the lower-atmosphere at the footpoints of flare loops. Light curves in these wavelengths exhibit an impulsive rise, followed by a gradual decay. Using the transition region DEMs computed as above, we find, as a *post-facto* confirmation of our initial assumption, that the UV 1600 Å band is indeed dominated by the C IV line. The emissivity $\epsilon(T)$ (radiated power in erg cm^{-3} s^{-1} divided by N_e^2) of the optically thin C IV multiplet is derived from CHIANTI 7.0 with ionization equilibrium (Dere et al. 1997; Landi et al. 2012). Using the DEM, the total C IV photon flux is computed in units of photons cm^{-1}s^{-1}sr^{-1} and by convolving with the AIA instrument response function, the flux is converted to observed count rate in units of DN s^{-1}. The right panel of Figure 9 shows the synthetic light curve of the C IV total counts summed up from foot-points of all flare loops, in comparison with the observed UV 1600 Å total counts. It is seen that, during the decay phase, the synthetic light curve agrees very well with the observed light curve in both the evolution timescale and the magnitude. However, the impulsive phases are significantly underestimated by the model calculations, because the equilibrium approximation is not adequate during the rise (heating) phase of the flare.

The He II 304 Å line is usually formed in mid transition region temperature plasma (in equilibrium conditions this would be close to 80,000 K). To understand the observed He II emission at the flare foot-points, we also calculate the contribution function of the He II line under conditions of statistical equilibrium, and convolved it with the transition region DEM and the AIA instrument's response function in this band. In Figure 9, the left panel shows the synthetic He II total counts light curve, which evolve along with the observed light curve with comparable amount of emission during the decay phase.

The successful comparison between the synthetic and observed C IV light curve during the decay phase confirms that the pressure-gauge approach reasonably describes the transition region during this phase. The similarity of the observed and computed light curves of He II 304 Å emission is remarkable, given the earlier work, particularly that of Laming & Feldman (1992), cited in the introduction.

3.4. He I 10830 Å

Our observations indicate that the He I 10830 Å line is formed somewhere in the stratified chromosphere. During the flare, this layer must be significantly heated to enhance the He I line against the continuum background. However, the chromosphere is an excellent thermostat, having enormous sinks of energy associated with latent heat of ionization of hydrogen and radiation losses. But if local heating exceeds a critical limit, then a thermal runaway to coronal temperatures is expected to occur, since once hydrogen is all ionized, a major sink of energy is lost (Judge 2010). Dumping of heat into the chromosphere bifurcates the temperature distribution such that either the temperature is below *approx* 8000 K or it

moves immediately, with a narrow transition region, to coronal temperatures. Since He I is rapidly ionized at coronal temperatures, we must look to the underlying chromosphere for the source of the 10830 photons during the flare.

Here we consider two pictures: the first is that EUV irradiation of the chromosphere from above ionized the neutral helium atoms. Then the recombination of the electrons and He II generates populations of the upper levels ($1s2p\ ^3P^o_{0,1,2}$) of the multiplet (Zirin 1975). The second is the "burst model" advocated by Laming & Feldman (1992).

The observed enhancements of 10830 Å range from 1.2 to 2.5 times the pre-flare emission (Figure 6): the median value is close to 1.3, which we now adopt. As mentioned above, most flare footpoints locate in the penumbra. Before the flare, the clear view of the sunspot penumbra indicates the shallow absorption in 10830 Å. Therefore, most flux comes from the photosphere in these area. So we approximate emission during this stage by the continuum emission. The total emission is estimated in physical units from 10830 Å as follows. The estimated continuum formation temperature at 10830 Å is around 6000 K at disk center as shown by Maltby et al. (1986). 5600 K is adopted since the flare footpoints locate in penumbra. Assuming that the continuum is generated by black-body radiation, we can write the excess intensity as

$$I_{ex} \approx (1.3 - 1.0) \times B_\lambda(5600\mathrm{K}) \times \Delta \quad \text{erg cm}^{-2}\text{sr}^{-1}\text{s}^{-1},$$

Where Δ is an (unknown) width of the excess emission line profile in wavelength units. Let $\Delta = fw$ where f is the ratio of the radiation emitted by all 10830 Å transitions divided by the fraction that we observe, which covers a width $w = 0.5$ Å. Values of $1 \leq f < 10$ seem reasonable values, we will use $f = 2$ since our bandpass cover almost half of the red component of 10830 Å spectrum. We have, using a photospheric radiation temperature near 5600 K $= 8 \times 10^5$ erg cm^{-2} sr^{-1} Å^{-1} s^{-1}, and $w = 0.5$ Å

$$I_{ex} \approx (0.3)\,2\,(0.5)\,8 \times 10^5 \quad \text{erg cm}^{-2}\text{sr}^{-1}\text{s}^{-1},$$

or a total 10830 Å energy flux out of the optically thin slab of

$$F_{ex} = 2\pi I_{ex} \approx 1.5 \times 10^6 \quad \text{erg cm}^{-2}\text{s}^{-1}.$$

Since the energy of one 10830 photon is 1.83×10^{-12} erg, the photon flux is then

$$N_{ex} \approx 0.8 \times 10^{18} \quad \text{ph cm}^{-2}\text{s}^{-1}.$$

3.4.1. Photoionization-recombination picture

If the typical 10830 Å enhancements are produced via the photoionization-recombination mechanism, the required energy flux of ionizing EUV photons is simply determined by computing the photoionization rate and the number of photons emitted in 10830 Å per ionization

(e.g., Zirin 1975). Unlike Zirin's work, we need not consider photoexcitation by the photosphere since the photospheric radiation cannot generate emission above its own continuum. Using the HAOS-DIPER package (Judge 2007), we find that between 32 and 62% of all recombinations lead to 10830 emission, depending on whether the 504 Å continuum is assumed optically thin or thick respectively. We adopt a value of 50% for optical depths close to unity where the bulk of the helium material will be photoionized. EUV photons at wavelengths below 504 Å are needed for photoionization of He I. We can estimate the photon energy flux at 500 Å, which is the minimum required flux to generate the observed enhancement in the photoionization-recombination picture, as

$$N_{EUV} = N_{ex}/0.5 = 1.6 \times 10^{18} \quad \text{ph cm}^{-2}\text{s}^{-1},$$

for an energy flux of

$$F_{EUV} \approx 6 \times 10^{7} \quad \text{erg cm}^{-2}\text{s}^{-1}.$$

When distributed over an area of 906 AIA pixels, we find a total luminosity of the flare at wavelengths close to and below 504 Å of 1.1×10^{26} erg s^{-1}. If distributed across the 9 patches, the average luminosity per patch is 1.2×10^{25} erg s^{-1}.

The solid lines in Figure 10 shows the estimated photon energy flux from the observed IR enhancement in each of the 8 patches. P5 is not plotted since its emission is blended with the absorption from the nearby filament. With the transition region DEM computed for every pixel, we estimate the total optically-thin radiation energy by transition region plasmas of up to 2 MK, as plotted in dotted lines in Figure 10. It is seen that, in most of these patches, the estimated radiation energy is comparable with the required photon energy to generate the enhanced IR emission during the decay phase for as long as observed. We conclude that photoionization by EUV photons in the overlying transition region is a viable mechanism for the prolonged He I emission at the flare foot-points.

An independent EUV photon energy flux produced in this flare can be estimated from observations by the Extreme Ultraviolet Variability Experiment (EVE; Woods et al. 2012) on SDO. Two EVE spectrographs measure the whole-Sun solar extreme ultraviolet (EUV) radiation spectrum from 10-1050 Å with a resolution of approximately 1 Å and a cadence of 10 seconds. During this flare the "A" spectrograph on EVE acquired data in the range 60-380 Å, no data above 380 Å were obtained with the "B" spectrograph. The net EUV flux from the flare, obtained by subtraction of pre-flare emission, is shown in Figure 11. The solid line is the total flux observed by EVE from 60-380 Å while the dotted line is the calculated total optically-thin radiation by plasmas of up to 2 MK. The observed and measured fluxes are within ± a factor of three. Given the crude nature of the calculations and complex geometry of the flaring plasmas at various wavelengths, these measurements provide reassurance that the photon fluxes in the model are broadly compatible with the data.

Laming & Feldman (1992) estimate $2 - 8 \times 10^{16}$ photons cm^{-2} s^{-1} sr^{-1} for the EUV ionizing intensity in the He I and He II continua. The number directed towards the chromo-

sphere is 2π larger, or $\sim 3 \times 10^{17}$ photons cm^{-2} s^{-1}. This is a factor of 7 smaller than our estimate. This difference may be real, reflecting different flares, or it may reflect differences in the resolution of instruments used. Our data has a far higher angular resolution, necessarily leading to higher intensities as smaller flare kernels are better resolved.

3.4.2. Burst picture

The essence of this picture is that a burst of heating is assumed to occur in cool (chromospheric) plasma on time scales small compared with the time taken to ionize a given ion. During the burst the electron temperature is raised above the quiescent state, the hotter electrons lead to line emission before the ions involved become ionized. Heuristic arguments for this model have been given for EUV/UV helium lines by Laming & Feldman (1992). It has been placed on firmer theoretical grounds by Judge (2005). In the work of Laming and Feldman, burst temperatures near 1.8×10^5 K were needed to reproduce spectra of He II which are consistent with spectra of He I.

This picture seems unlikely to be able to explain the 10830 Å line's behavior reported here for the following reasons. The He I ionization times for pre-flare electron densities of around 5×10^{10} cm^{-3} (the value in the pre-flare upper chromosphere from Vernazza et al. 1981) are about 100, 2 and 0.05 s for burst electron temperatures of 2.3×10^4, 4.6×10^4, and 9.3×10^4 K ($\equiv$ 2, 4 and 8 eV), respectively. These values are simply scaled from Laming & Feldman's Figure 1. Excitation of the $1s2p\ ^3P^o$ levels by electron collisions naturally requires time scales with a similar temperature dependence because these levels lie at 21 eV, close to the continuum which is at 24.5 eV. Thus, populating these levels also leads to significant ionization. Further, a mere 1-2 eV is sufficient to ionize 50% of He I when photoionization from the $n = 2$ levels is considered (Laming & Feldman table 4). There are two difficulties: there is "little room in temperature space" where electron collisions from below can provide significant populations of the $1s2p\ ^3P^o$ levels- if they are excited, the He I is also readily ionized; for electron temperatures equivalent to 4 eV or more, needed to provide significant populations of these levels, the ionization times are so short so that one must invoke very many bursts to maintain the observed light curves, even during the "impulsive" rise phases (many tens of seconds for 10830 Å, see Figure 7).

Thus, recombination appears the only way to significantly populate the $1s2p\ ^3P^o$ levels. If this occurs via EUV photons, helium is selectively enhanced by the process outlined above. If however electron collisions are responsible, then one would expect very bright UV and EUV emission from trace species such as C, N, O, Si... from the upper chromosphere. Simultaneous observations of UV emission lines of various ions, for example from the new IRIS spacecraft, would be needed to see if pictures involving electron impact excitation of He I from the $1s^2\ ^1S$ level can be refuted or must be considered further.

4. DISCUSSIONS AND CONCLUSIONS

With the NST's high spatial resolution imaging observations as well as simultaneous space data from AIA on board SDO, we have given a detailed analysis of a C class flare observed continuously by all instruments at the cadence of 10-24 s (30 s for the TiO NST data). Specifically, we have tried to identify the dominant mechanism that produces the observed He I 10830 Å emissions.

We adopt the picture that the flare energy released in the corona propagates downwards by heat conduction and radiation into the underlying chromosphere. Particle beams seem insignificant on the basis that HXR fluxes are very small for this flare. Furthermore, our analysis focus on the decay phase of the flare, when the thermal model is sufficient for fitting the RHESSI spectra (Liu 2014). We compute the conductive downflow by determining heating rates inferred from 906 UV brightened pixels and the zero-dimensional EBTEL model to compute mean plasma properties in the corona and transition region of flare loops anchored within these pixels. Remarkably, the method can reproduce not only the C IV emission generated in the transition region at the flare foot-points, but also He II 304 Å emission, at least during the decay phases, to within a factor of two or so. This is remarkable agreement given the need to appeal to different mechanisms for bigger flares in previous work (Laming & Feldman 1992).

In terms of the He I 10830 Å multiplet, we argue that the downward propagation of energy via EUV photons is an important mechanism for excitation during the flare. Thus photo-ionization followed by recombination (PR; Zirin 1975) appears to be a prominent component exciting the 10830 Å multiplet during this event. Several pieces of evidence support this picture. Firstly, the morphology of the footpoint 10830 Å emission is qualitatively similar to a mixture of EUV channels observed with AIA. Secondly, the light curve of 10830 Å emission is, during the rise phase, similar to the (E)UV transition region light curves (304 Å and C IV which dominates the 1600 Å channel); during the decaying phases, it is perhaps more similar to the coronal SXR and EUV light curves. Thirdly, photon budgets are in reasonable agreement, as measured against both EVE data as well AIA data. Fourthly, the EUV radiation computed from the EBTEL models is also compatible with the photon budget for exciting 10830 Å via PR, during the decay phase.

In Andretta et al. (2008), the calculated helium spectrum is strongly affected by the spectral distribution and overall level of EUV coronal back-illumination, which is consistent with our result. They also found that He I 10830 Å is not sensitive to chromospheric helium abundance. In our calculation the helium abundance merely needs to be large enough so that it dominates most of the absorption of some EUV radiation, these photons being converted to longer wavelengths such as the 10830 Å line we computed down to the layer where EUV no longer penetrate. Our calculations are therefore insensitive to modest changes in the abundance of helium.

But there is perhaps one problem with the PR mechanism: if this were the *only* source of photons in 10830 Å, then there should be a close correspondence between the spatial distribution of the EUV photoionizing radiation and the underlying 10830 Å flare emission. However, this is not always the case. Scatter plots of peak intensities of the light curves in AIA 1600 Å, AIA 304 Å and He I 10830 Å show little correlation. One cause of the enormous scatter might be the fact that we observe only a 0.5 Å wide part of the 10830 Å line, shifted by 0.25 Å blueward of the line center. Therefore the morphology and light curves might contain velocity-dependent information that is not present in the broad band (E)UV channels.

Nevertheless, we also examined a "burst" picture which depends on non-equilibrium ionization to explain the large populations of the $n = 2$ triplet levels of helium. We concluded that this seems unlikely for the He I 10830 Å multiplet on several grounds, at least for the decay phases. Occam's Razor would compel us to accept the PR mechanism as perhaps the "simplest answer compatible with the data".

The assumed steady-state and equilibrium conditions are not adequate for calculations during the impulsive phases with durations of 10-100 seconds or so. In this period, the 10830 Å have identical rapid enhancement with the (E)UV lines. Perhaps a "burst" picture would be successful during this phase. Further observations including more UV lines, such as can be observed with IRIS, would be desirable, since to leading order the lines would respond to bursts but not the PR mechanism.

We thank BBSO observing staff and instrument team for their support. We thank Dr. Haisheng Ji for providing the narrow-band 10830 Å Lyot Filter. We are grateful to Giuliana de Toma for a careful reading of the paper. SDO is a project of NASA. Z. Z. and W. C. acknowledge the support of the US NSF (AGS-0847126, AGS-1146896 and AGS-1250818) and NASA (NNX13AG14G). J. Q. acknowledges the support by NSF (ATM-0748428) and NASA (NNX14AC06G). P. J. acknowledges the support by Montana State University Physics department, and the ASP and HAO programs at NCAR. NCAR is sponsored by the National Science Foundation. We thank the referee for carefully reading our paper and for providing valuable suggestions which substantially helped improving the quality of the paper.

REFERENCES

Andretta, V., Jordan, S. D., Brosius, J. W., et al. 2000, ApJ, 535, 438

Andretta, V., Mauas, P. J. D., Falchi, A., & Teriaca, L. 2008, ApJ, 681, 650

Avrett, E. H., Fontenla, J. M., & Loeser, R. 1994, in IAU Symposium, Vol. 154, Infrared Solar Physics, ed. D. M. Rabin, J. T. Jefferies, & C. Lindsey, 35

Cao, W., Coulter, R., Gorceix, N., & Goode, P. R. 2010a, in Society of Photo-Optical Instrumentation Engineers (SPIE) Conference Series, Vol. 7742, Society of Photo-Optical Instrumentation Engineers (SPIE) Conference Series

Cao, W., Gorceix, N., Coulter, R., et al. 2010b, Astronomische Nachrichten, 331, 636

Cao, W., Gorceix, N., Coulter, R., et al. 2010c, in Society of Photo-Optical Instrumentation Engineers (SPIE) Conference Series, Vol. 7735, Society of Photo-Optical Instrumentation Engineers (SPIE) Conference Series

Cargill, P. J., Bradshaw, S. J., & Klimchuk, J. A. 2012a, ApJ, 752, 161

—. 2012b, ApJ, 758, 5

Centeno, R., Trujillo Bueno, J., Uitenbroek, H., & Collados, M. 2008, ApJ, 677, 742

Dere, K. P., Landi, E., Mason, H. E., Monsignori Fossi, B. C., & Young, P. R. 1997, A&AS, 125, 149

Fisher, G. H. 1987, ApJ, 317, 502

—. 1989, ApJ, 346, 1019

Fletcher, L., Dennis, B. R., Hudson, H. S., et al. 2011, Space Sci. Rev., 159, 19

Goode, P. R., & Cao, W. 2012, in Society of Photo-Optical Instrumentation Engineers (SPIE) Conference Series, Vol. 8444, Society of Photo-Optical Instrumentation Engineers (SPIE) Conference Series

Griffiths, N. W., Fisher, G. H., & Siegmund, O. H. W. 1998, in Astronomical Society of the Pacific Conference Series, Vol. 154, Cool Stars, Stellar Systems, and the Sun, ed. R. A. Donahue & J. A. Bookbinder, 621

Hannah, I. G., Christe, S., Krucker, S., et al. 2008, ApJ, 677, 704

Harvey, K. L., & Recely, F. 1984, Sol. Phys., 91, 127

Hawley, S. L., & Fisher, G. H. 1992, ApJS, 78, 565

Hawley, S. L., Allred, J. C., Johns-Krull, C. M., et al. 2003, ApJ, 597, 535

Jordan, C. 1975, MNRAS, 170, 429

—. 1980, A&A, 86, 355

Judge, P. G. 2005, J. Quant. Spec. Radiat. Transf., 92, 479

Judge, P. G. 2007, in The HAO Spectral Diagnostic Package for Emitted Radiation (HAOSDIPER) Reference Guide (Version 1.0), Technical Report NCAR/TN-473-STR, National Center for Atmospheric Research

—. 2010, Mem. Soc. Astron. Italiana, 81, 543

Judge, P. G., & Pietarila, A. 2004, ApJ, 606, 1258

Kleint, L. 2012, ApJ, 748, 138

Klimchuk, J. A., Patsourakos, S., & Cargill, P. J. 2008, ApJ, 682, 1351

Laming, J. M., & Feldman, U. 1992, ApJ, 386, 364

Landi, E., Del Zanna, G., Young, P. R., Dere, K. P., & Mason, H. E. 2012, ApJ, 744, 99

Lemen, J. R., Title, A. M., Akin, D. J., et al. 2012, Sol. Phys., 275, 17

Li, H., You, J., Yu, X., & Du, Q. 2007, Sol. Phys., 241, 301

Li, Y., Qiu, J., & Ding, M. D. 2014, ApJ, 781, 120

Lin, R. P., Dennis, B. R., Hurford, G. J., et al. 2002, Sol. Phys., 210, 3

Liu, W.-J. 2014, Determining Heating Rates in Reconnection Formed Flare Loops, PhD thesis, Department of Physics, Montana State University, Montana, USA

Liu, W.-J., Qiu, J., Longcope, D. W., & Caspi, A. 2013, ApJ, 770, 111

Maltby, P., Avrett, E. H., Carlsson, M., et al. 1986, ApJ, 306, 284

Penn, M. J., & Kuhn, J. R. 1995, ApJ, 441, L51

Pesnell, W. D., Thompson, B. J., & Chamberlin, P. C. 2012, Sol. Phys., 275, 3

Pietarila, A., & Judge, P. G. 2004, ApJ, 606, 1239

Pozhalova, Z. A. 1988, Soviet Ast., 32, 542

Qiu, J., Liu, W.-J., & Longcope, D. W. 2012, ApJ, 752, 124

Qiu, J., Sturrock, Z., Longcope, D. W., Klimchuk, J. A., & Liu, W.-J. 2013, ApJ, 774, 14

Schou, J., Scherrer, P. H., Bush, R. I., et al. 2012, Sol. Phys., 275, 229

Tandberg-Hanssen, E. 1967, Solar activity

Trujillo Bueno, J., & Asensio Ramos, A. 2007, ApJ, 655, 642

Vernazza, J. E., Avrett, E. H., & Loeser, R. 1981, ApJS, 45, 635

Wöger, F., & von der Lühe, O. 2007, Appl. Opt., 46, 8015

Woods, T. N., Eparvier, F. G., Hock, R., et al. 2012, Sol. Phys., 275, 115

Zirin, H. 1975, ApJ, 199, L63

This preprint was prepared with the AAS LaTeX macros v5.0.

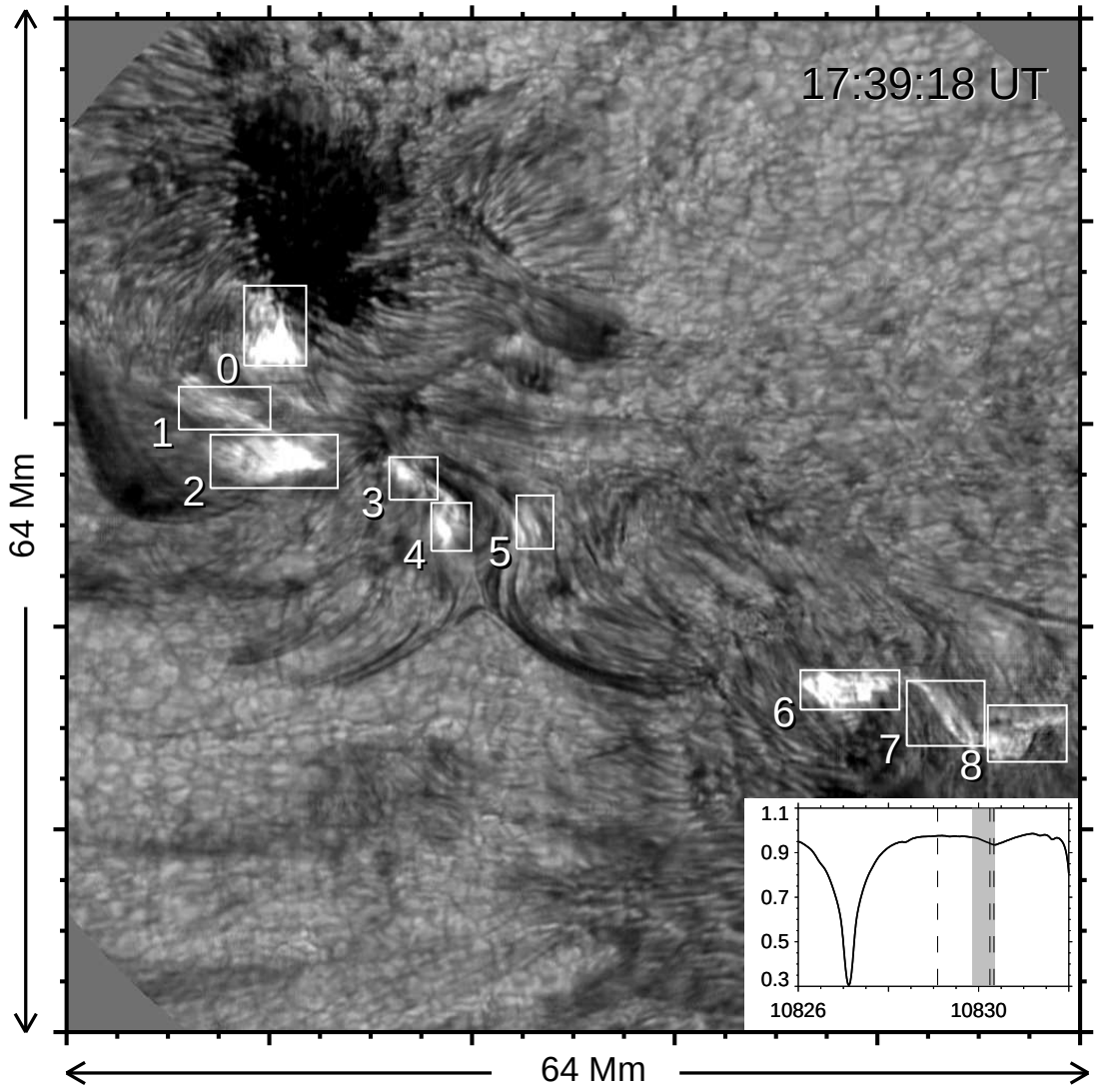

Fig. 1.— Snapshot of the He I 10830 Å observation. The bandpass of the narrow-band filter is illustrated by a vertical strip in the solar spectrum on the lower right corner, and three vertical dashed lines depict the line centers of the He I 10830 Å triplets. The field of view is 64 Mm × 64 Mm. The 9 small boxes with digits encompass the footpoints of the flare during its second peak.

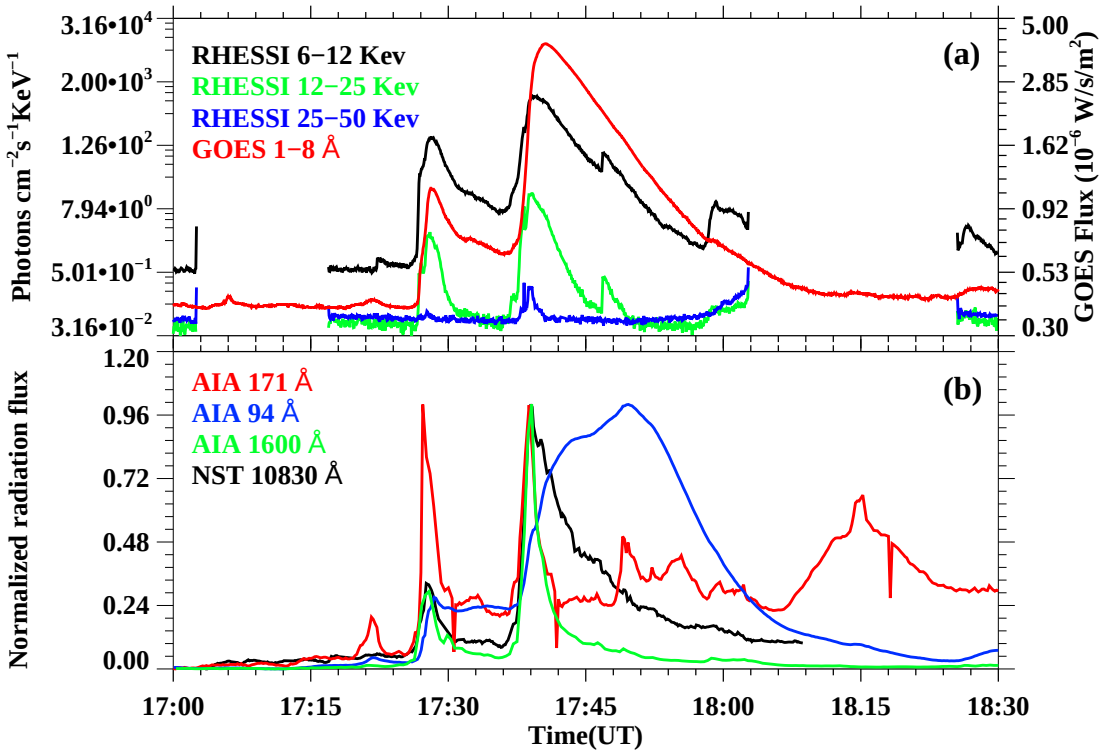

Fig. 2.— Light curves of the 2012 June 17 C3.9 flare. Both soft X-ray 1-8 Å from GOES and some X-ray flux from RHESSI are shown in panel a. Time profiles in UV 1600 Å and EUV 171 Å and 94 Å by AIA/SDO are plotted in panel b. Also plotted is the light curve of 10830 Å.

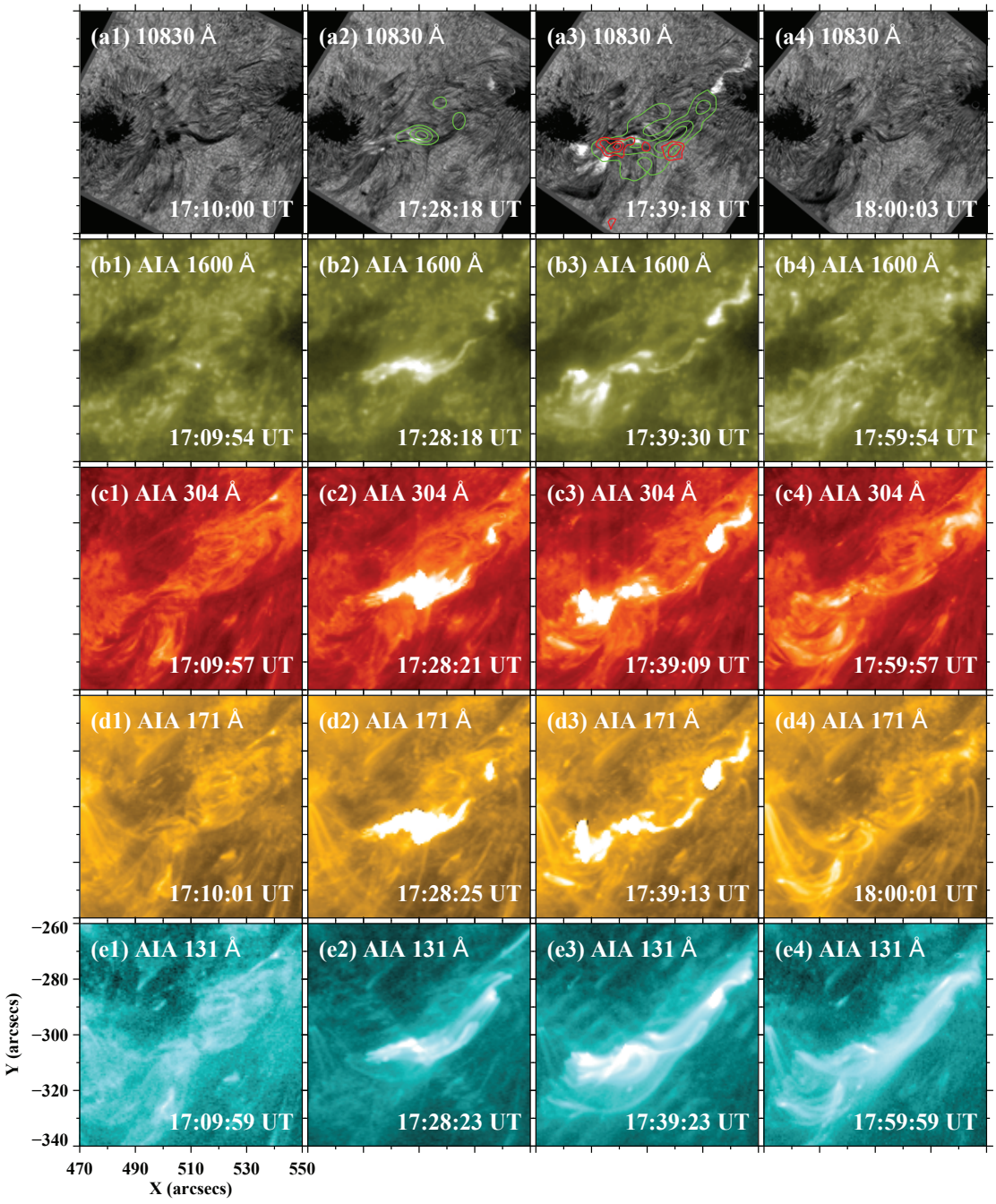

Fig. 3.— Snapshots of the flare in a few bands at a few moments with the same field of view. Rows from top to bottom: He I 10830 Å, UV 1600 Å, EUV 304 Å, 171 Å and 131 Å. Left panels (a1-e1): snapshots before the filament eruption. Middle panels (a2-e2): snapshots during the first peak of the flare. Panels (a3-e3): snapshots during the second peak of the flare. Right panels (a4-e4): snapshots after the flare. The contours on the 10830 Å filtergrams are from RHESSI images with channels of: 6-15 keV (green) and 25-50 keV (red). The RHESSI images are made from 17:28:10 UT with 10 seconds integration and from 17:38:30 UT with 1 minute integration, respectively. The contour levels are 90%, 75% and 60% of the peak intensity of each image.

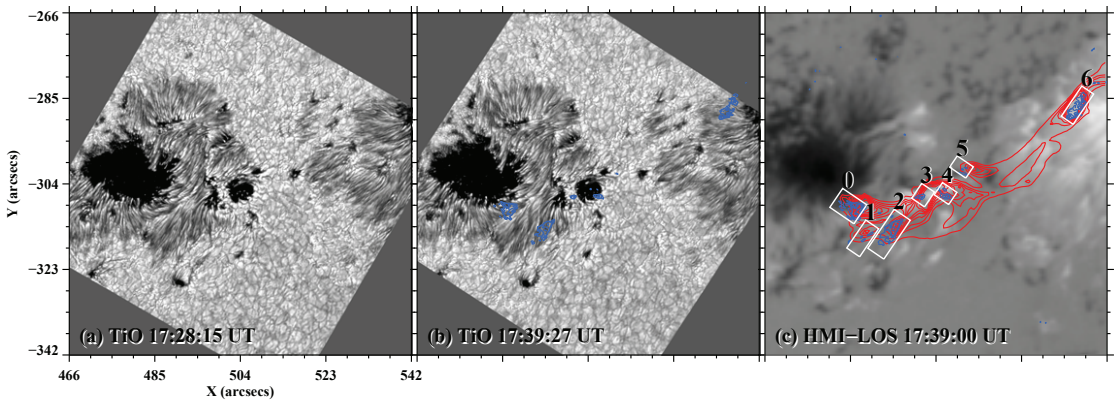

Fig. 4.— Panel (a) and (b): TiO images from NST/BBSO during the two impulsive phase. Blue contours on panel (b) are regions of emission measured in He I 10830 Å. Panel (c): HMI line-of-sight (LOS) magnetogram overlaid with foot-point contour in 10830 Å (Blue) and loop contour in 131 Å (Red). The boxes encompass the patches indicated in Figure 1. Three panels have the same field of view of $76'' \times 76''$.

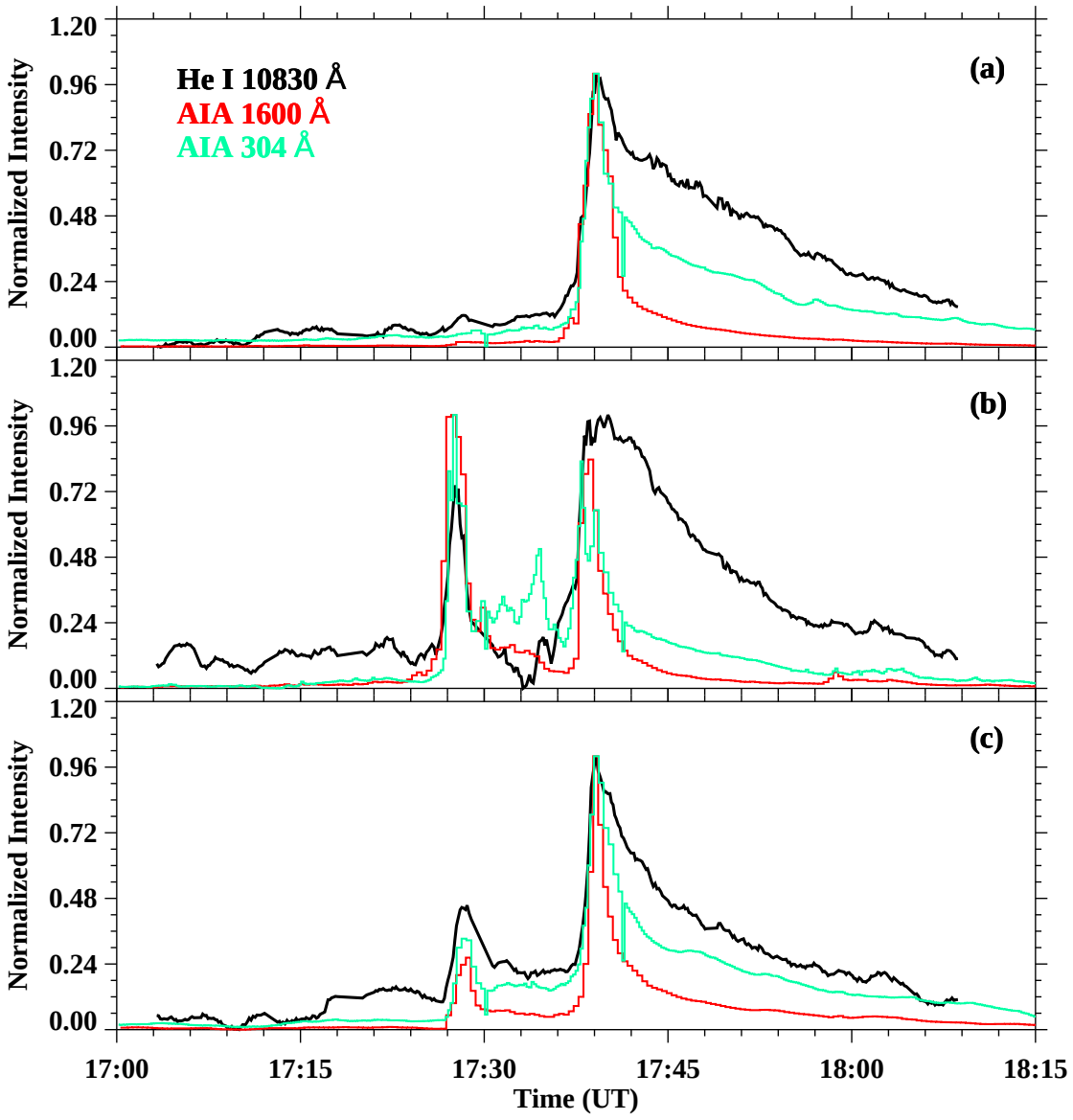

Fig. 5.— Light curves in He I 10830 Å, AIA 1600 Å and 304 Å. Panel a to c represent for patches 0, 4 and 6 noted in Figure 1, respectively. The minimum value is subtracted from each light curve, which then normalized to its maximum.

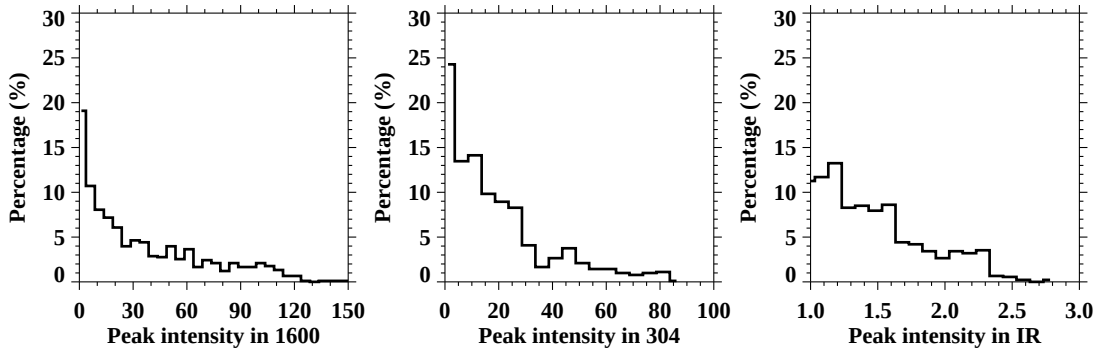

Fig. 6.— Histogram of peak intensities for all the footpoint pixels: x axis shows peak intensities as how many times the pre-flare intensity; y axis is in percentage. For the He I 10830 Å, the pre-flare intensity is approximated by the quiescent continuum.

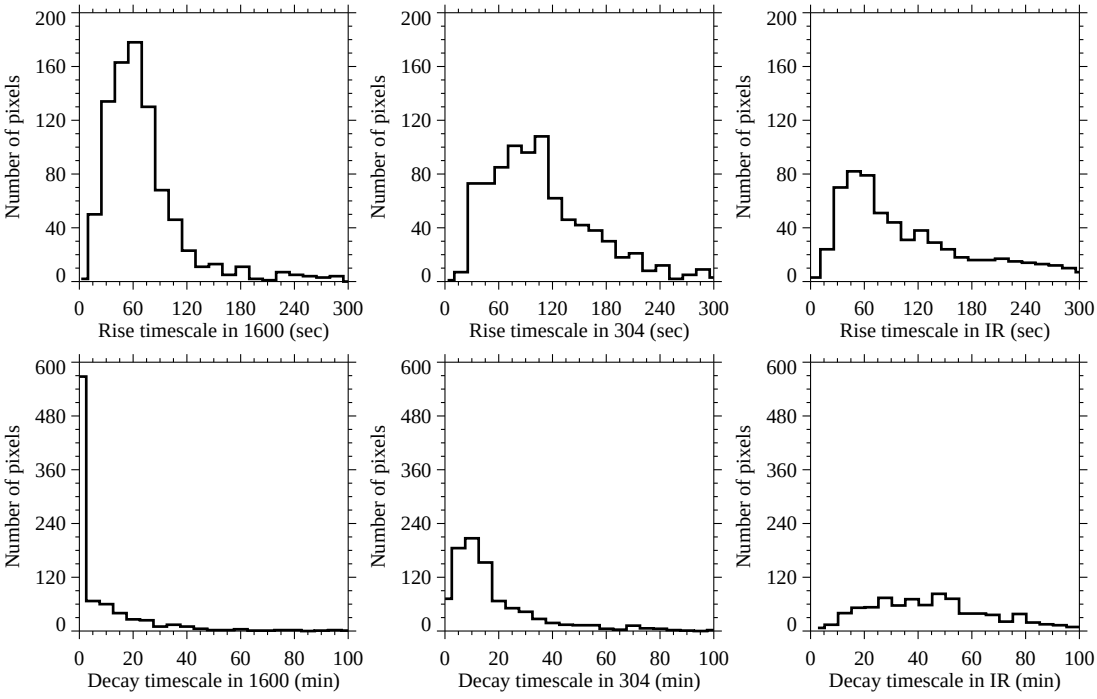
Number of pixels
Rise timescale in 1600 (sec)
Rise timescale in 304 (sec)
Rise timescale in IR (sec)
Decay timescale in 1600 (min)
Decay timescale in 304 (min)
Decay timescale in IR (min)

Fig. 7.— Histogram of 10830 Å, 1600 Å and 304 Å rise and decay timescales. Upper panels: rise timescales. Bottom panels: decay timescales.

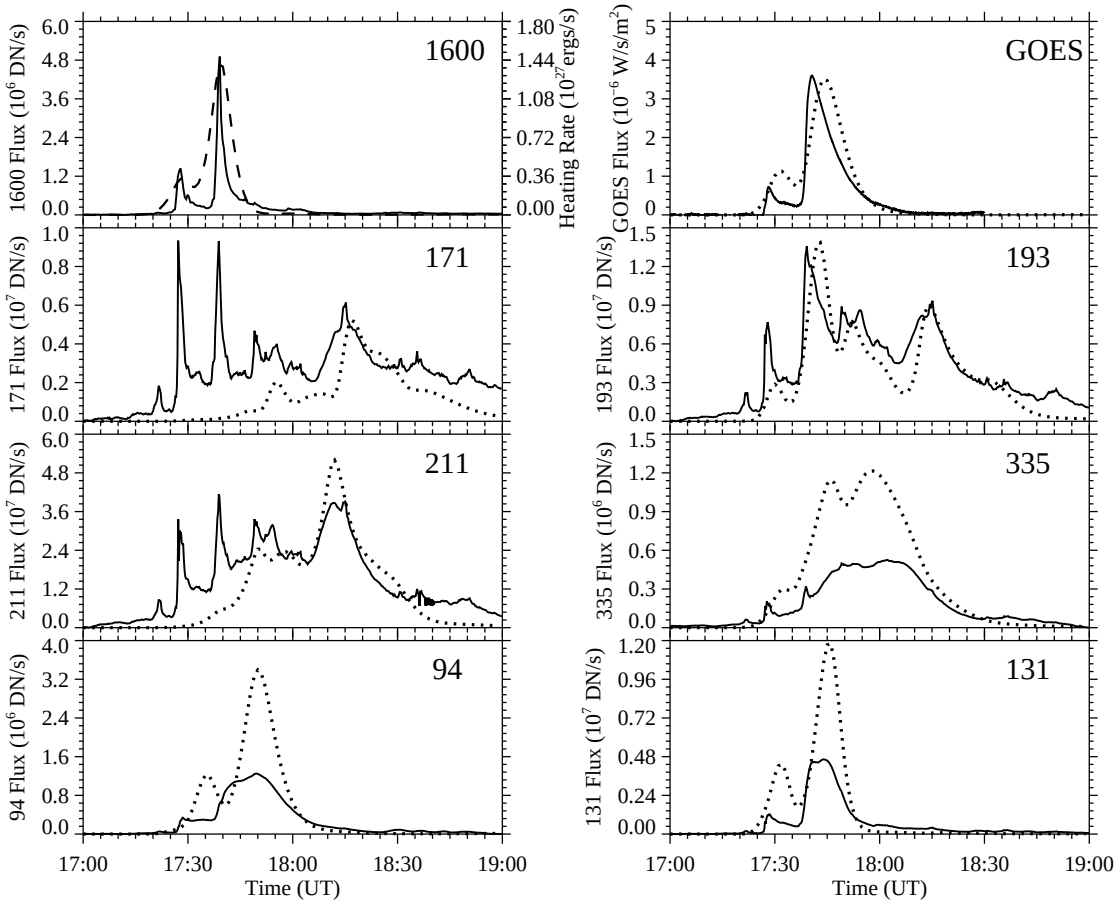

Fig. 8.— Comparison of observed and synthetic flux calculated through EBTEL model. The dotted and solid lines are the synthetic and observed light curves, respectively. The heating rate is given as the dashed light curve in the top left panel. The corresponding passbands are noted by the number on the right corner of each panel.

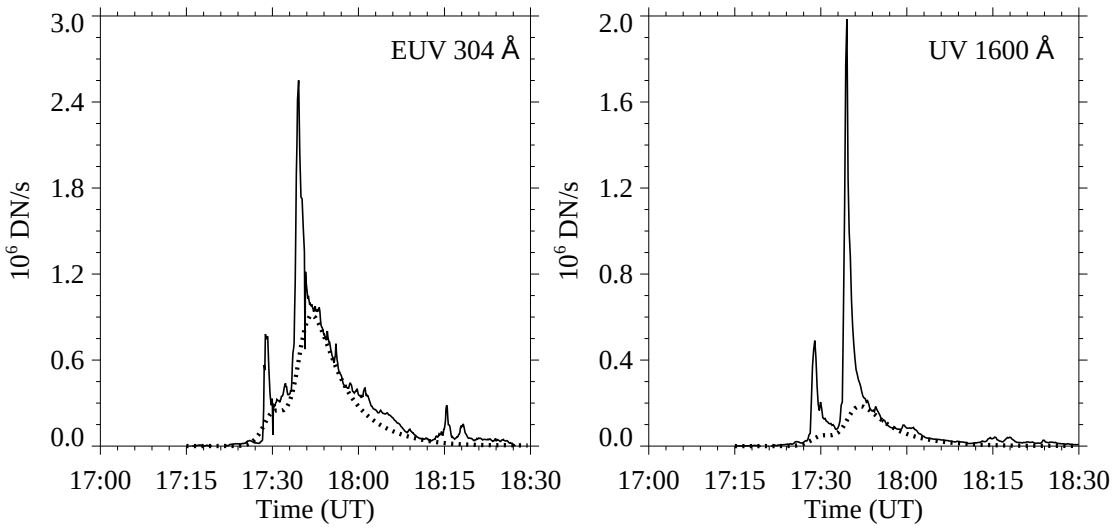

Fig. 9.— Dotted lines: computed light curves for 304 and 1600 Å with pressure gauge assumption. Solid lines: observed data.

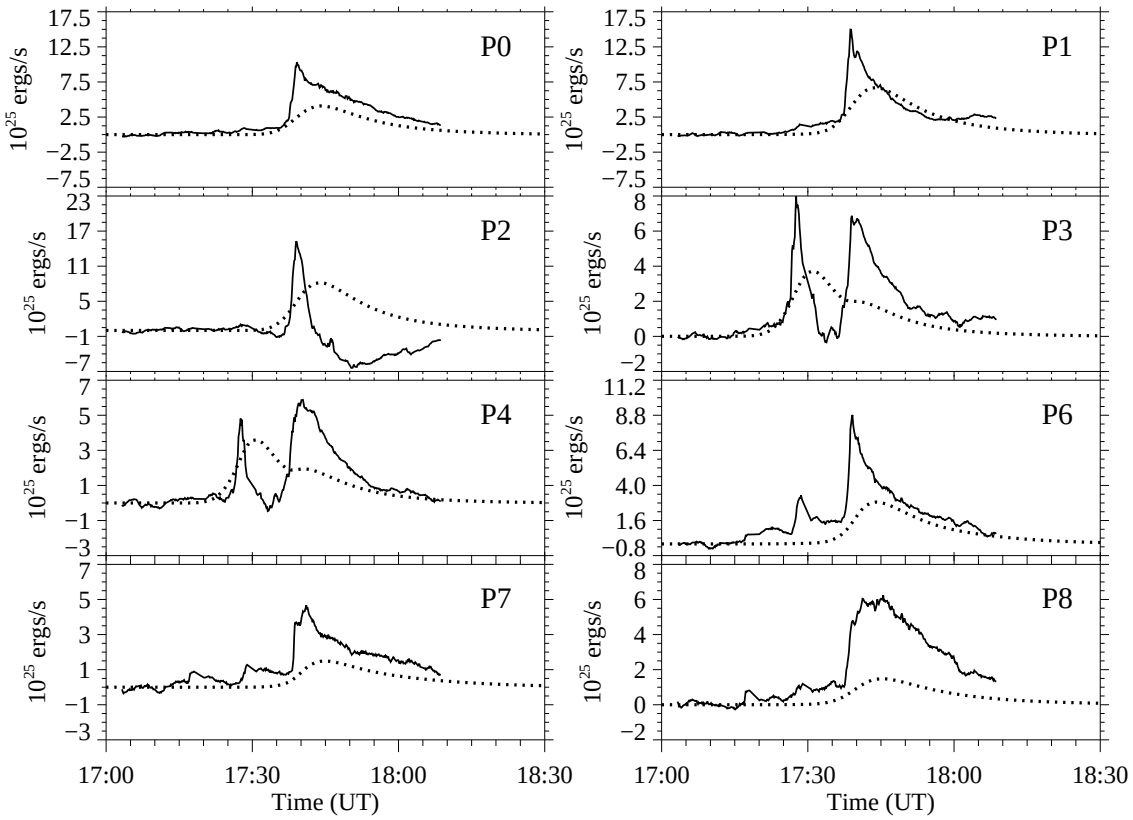

Fig. 10.— Total estimated optically-thin energy flux from the transition region (dotted line) compare with estimation from 10830 Å enhancement (solid line). The number on the upper right conner of each panel denotes the patches showed in Figure 1. The patch P5 is not plotted here because the emissions are blended with the filament absorption.

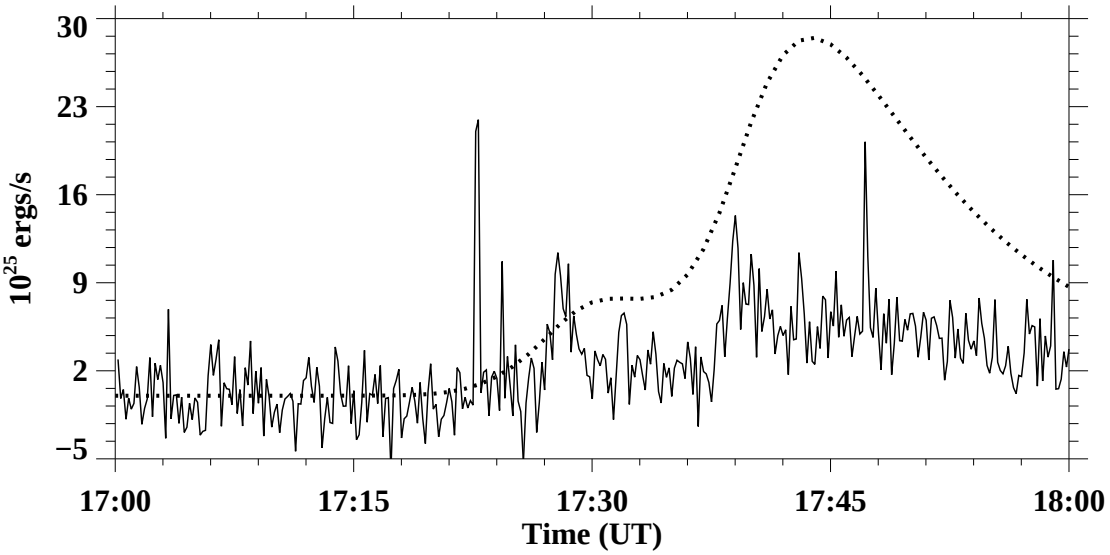

Fig. 11.— Solid line: EVE observed EUV flux summed up through the spectrum range from 60-380 Å with pre-flare emission subtracted. Dotted line: model estimated total optically-thin radiation flux with pressure-gauge approximation.